Numerical Simulation of Laser Induced Plasma During Pulsed Laser Deposition

Zhaoyan Zhang

Department of Mechanical Engineering-Engineering Mechanics

Michigan Technological University

Houghton, MI 49931

Zhen-Xue Han and George S. Dulikravich

Department of Mechanical and Aerospace Engineering

The University of Texas at Arlington

Arlington, TX 76019

Abstract

A numerical study of the laser induced evaporation and ionization process during pulsed laser deposition is presented. The process is separated into three domains: i) conduction inside the solid, ii) a discontinuity layer between solid and vapor, and iii) expansion of high temperature vapor/plasma. A quasi-one-dimensional model is solved to predict the temperature field inside solid. Mass, momentum and energy are conserved across the discontinuity layer. Equations of mass, momentum and energy conservation are solved simultaneously to provide boundary conditions for the expansion process. Euler equations are used to model the expansion of high temperature vapor/plasma. The Euler equations are integrated numerically using a Runge-Kutta scheme combined with flux vector splitting. The density, pressure, temperature and velocity contours of the vapor phase are calculated and the results are analyzed.

Introduction

One important aspect of laser-material interaction of interest is the application of lasers in the field of material processing. During the laser material processing, the laser energy is absorbed within a short penetration depth of the material. This leads to an increase of the surface temperature. When the laser energy is sufficiently high, evaporation of the material occurs. The vapor generated can be ionized to create a high density plasma. This high temperature, high pressure vapor/plasma can be harnessed to produce thin films. This so-called pulsed laser deposition (PLD) has raised interest as a promising technique for deposition of high T_c superconductor[1], semiconductor[2], diamond-like-carbon[3], and a wide range of other materials. However, many problems remain. For example, low deposition rate and deposition of particulates needs to be better understood. The microstructure and the properties of the thin films depend very much on the deposition conditions, *e.g.*, the laser intensity and back pressure of the vacuum chamber. A good understanding of the mechanism of the laser induced vapor/plasma is needed to determine the necessary parameters for this process. The evaporation process of a solid was first studied by Ready[4] in the 1960s. When the laser pulse duration is in the microsecond range or longer and the power density of the laser is less than 10^6 W/cm^2, vaporization is the predominant mode of removal. It has been shown[5] that

the surface temperature will rise logarithmically with increasing intensity of laser light, while the surface ablation rate increases linearly with the laser intensity barring heat losses. The evaporation process into an atmospheric environment may be analyzed more precisely by taking account of a Knudsen layer adjacent to the solid surface. Through this boundary layer the vapor expands into a rarefaction wave. This process has been studied by Anisimov[6] and Knight[7]. In the pioneering work of Krokhin[8], the physical mechanism of evaporation coupled with expansion of vapor and plasma was formulated. These effects have since been investigated in great detail both theoretically and experimentally ($e.g.,$ Material Research Society Symposium Proceedings[9] and Workshop on Laser Interaction and Related Plasma Phenomena[10]).

Preliminary numerical simulations of laser-target interaction have been conducted by many researchers as well. Tokarev $et\ al.$[13] proposed an analytical thermal model of ultraviolet laser ablation. It took into account the factors which had not been treated analytically simultaneously before. These factors are i) the moving interface; ii) an Arrhenius dependence of ablation rates; iii) the shielding of the laser-irradiated surface by plume and/or plasma; iv) the temperature dependence of optical constants of the irradiated materials; v) thermal conductivity effects on ablation kinetics. The initiation and expansion of the laser induced plume/plasma

were not studied and the shielding of the solid surface by the plume/plasma was modeled approximately. Ho *et al.*[11,12] studied the heat transfer and fluid flow phenomena, and subsequent ionization of laser induced plume/plasma during pulsed laser processing of metals. The rates of ionization were computed using Saha's equation. Inverse *bremsstrahlung* absorption was considered as the main mechanism of plasma absorption.

In the previous studies, The treatment of the solid-vapor interface and the plasma emission are simplistic. It also appears that some equations in the electrostatic system of units are used directly and are not properly converted, while the model apparently uses an MKSCK system of units. In the present paper, a numerical study of laser induced vapor/plasma during pulsed laser deposition of diamond-like-carbon is presented. The laser induced evaporation and ionization is separated into three domains: i) heat conduction inside the solid, ii) the evaporation wave attached to the solid surface, and iii) expansion of the high temperature vapor. Heat conduction inside the solid is modeled using a quasi-one-dimensional approach. The conduction equation is then solved approximately using an integral method. In the solid-vapor interface, the evaporation wave results in a discontinuity similar to a shock wave. Conservation of mass, momentum and energy is used to relate the properties of the solid and vapor phase. The expansion and ion-

ization process of the high temperature vapor is modeled by Euler equations. It is assumed that the degree of ionization follows Saha's equation and that plasma obeys the ideal gas law. Strong absorption of laser light by the ionized gas is predominantly due to free-free transition of electrons in collision with positive ions, and is modeled using inverse $Bremsstrahlung$ absorption. A two-step Runge-Kutta scheme together with a second-order flux vector splitting scheme proposed by van Leer[14,15] is used to calculate the flow field and to capture the location of the shock wave resulting from the expansion of plasma.

Problem Formulation

The laser-induced vaporization and ionization process can be separated into three domains: i) conduction inside the solid, ii) an evaporation wave attached to the solid surface, iii) expansion of high temperature vapor. A sketch for the problem under consideration is given in Figure 1. The heat diffusion process can be described by a transient quasi-one-dimensional model.

$$\frac{\partial T}{\partial t} - v_{n,0}\frac{\partial T}{\partial n} = \frac{1}{\rho_0 c_p}\left[\frac{\partial}{\partial n}\left(k\frac{\partial T}{\partial n}\right) - \left(\frac{\partial Q_l}{\partial z_s}\right)\right], \tag{1}$$

where t is time, z_s is the coordinate in the direction of laser beam, n is the coordinate in the direction of the local surface normal, $v_{n,0}$ is the ablation velocity

into the negative n direction, $k/\rho_0 c_p$ is the thermal diffusivity (α_s) of the solid material, $Q_l = (1-R)Q_s e^{-\kappa[z_s - s(r,t)]}$ is the laser flux penetrating into the condensed phase, Q_s is the laser flux at the surface of the condensed phase, R is the reflectance of the solid.

The boundary conditions are

$$z_s = s(r,t) \quad : \qquad k\mathbf{n}\cdot\nabla T = \rho_0 L v_{n,0}, \tag{2}$$

$$z_s \to \infty \quad : \qquad T \to T_\infty \tag{3}$$

$$t = 0 \quad : \qquad T = T_\infty \tag{4}$$

where L is the latent heat of the material, ρ_0 is its density, and T_∞ is the ambient temperature.

The ablation velocity $v_{n,0}$ is governed by an Arhennius equation[5]

$$v_{n,0} = \frac{P_b \exp\left(\frac{L}{R}(1/T_b - 1/T_s)\right)}{\rho_0\sqrt{2\pi k_B T_s/m}} \tag{5}$$

$$= \frac{P_0}{\rho_0\sqrt{2\pi k_B T_s/m}}, \tag{6}$$

where m is the mass of an evaporating molecule, k_B is Boltzmann's constant, T_s is the surface temperature, R is the gas constant, and P_b is the saturation pressure

at the equilibrium boiling temperature T_b, P_0 is the vapor pressure at the surface temperature.

The evaporation wave results in a jump condition similar to a shock wave. This region is a Knudson layer with a thickness of only a few mean free paths and is attached to the receding surface. The Knudsen layer obeys the laws of conservation of mass, momentum and energy, which can be expressed as[8]

$$-\rho_0 v_{n,0} = \rho_1(v_{n,1} - v_{n,0}), \tag{7}$$

$$P_0 = P_1 - \rho_0 v_{n,0} v_{n,1}, \tag{8}$$

$$-\rho_0 v_{n,0} e_0 = -\rho_0 v_{n,0}(e_1 + {v_{n,1}}^2/2) + P_1 v_{n,1}, \tag{9}$$

where ρ is the density, e is the mass-specific internal energy, and P is the pressure. The subscript 0 indicates values for the condensed phase, and subscript 1 indicates values for the gaseous phase. The values for the condensed medium are derived from the heat diffusion process, and $v_{n,0}$ is obtained from Equation (6). e_0 is related to the surface temperature by the state equation $e_0 = C_v T_s$, and the vapor pressure is related to its density and temperature by the ideal gas law $P_1 = \rho_1 R T_1$. Note that quasi-one-dimensional forms of the conservation laws are used, again because the thickness of the evaporation wave front is of only a few mean free

paths. As in a shock wave, the temperature and velocity gradient is confined to the interior of the evaporation wave, therefore, the velocity and temperature on either side of the wave while different have no effects on each other.

The expansion process of the high temperature vapor can be modeled by the following equations

$$\frac{\partial \rho}{\partial t} + \nabla \cdot (\rho \mathbf{u}) = 0, \tag{10}$$

$$\rho \frac{\partial \mathbf{u}}{\partial t} + \rho(\mathbf{u} \cdot \nabla)\mathbf{u} + \nabla P = 0, \tag{11}$$

$$\rho \frac{\partial \epsilon}{\partial t} + \rho \mathbf{u} \cdot \nabla \epsilon + P \nabla \cdot \mathbf{u} = \Lambda + W_l. \tag{12}$$

Here, ρ is the total density, $\mathbf{u}$ is the bulk fluid velocity, P is the pressure, ϵ is the mass-specific total energy of vapor/plasma. Λ is energy change due to ionization, and W_l is the heating due to the absorption of laser light. The specific total energy, ϵ, is related to its specific internal energy, e, by

$$\epsilon = e + \mathbf{u} \cdot \mathbf{u}/2. \tag{13}$$

The specific internal energy and pressure of vapor/plasma are given by

$$e = k_B T/[(\gamma - 1)m], \tag{14}$$

$$P = \rho k_B T/m, \tag{15}$$

where γ is the ratio of specific heats of the vapor/plasma.

The electron and ion number densities (n_e and n_i) are related to total number density (n) by Saha's equation (see, for example, Hughes[16])

$$\frac{n_e n_i}{n - n_i} = \frac{2(g_0)_i}{(g_0)_0} \left[\frac{2\pi m_e k_B T_e}{h^2}\right]^{3/2} \exp\left(-\frac{\chi_Z}{k_B T_e}\right), \tag{16}$$

where $(g_0)_i$ and $(g_0)_0$ are the statistical weights of ion and atom (degeneracy factors of ion and atom, respectively), and χ_Z is the ionization energy. The vapor/plasma heating due to the absorption of laser light W_l is given by

$$W_l = -\frac{\partial Q}{\partial z} = \alpha Q_0 e^{-\int_z^\infty \alpha z}, \tag{17}$$

where the absorption coefficient of the plasma is given by[16]

$$\alpha = \frac{n_i n_e {Z_i}^2 e^6 [1 - exp(-h\nu/k_B T_e)]}{24\pi^3 {\epsilon_0}^3 {m_e}^2 c h \nu^3} \left(\frac{me}{2h\nu}\right)^{1/2}. \tag{18}$$

The heat loss due to emission is negligible, because the plasma is extremely transparent to its own emission. Assuming a typical photon has a frequency of $\nu = cT_e/(2898\mu mK)$ (Wien's displacement law), the radiation mean free path for its own radiation is an order of magnitude larger than that for laser radiation[17]. The heat loss due to ionization is treated as a simple sink term, which is given by

$$\Lambda = -n_e \chi_Z. \tag{19}$$

There are four unknowns ρ, u_r, u_z and ϵ (others are related by algebraic equations) for an axisymmetric domain. At the solid surface, the results obtained from the evaporation wave front provide the vapor density, velocity and temperature, where $\rho = \rho_1$, $u_r = v_{n,1}\mathbf{n} \cdot \mathbf{r}$, $u_z = v_{n,1}\mathbf{n} \cdot \mathbf{z}$ and $\epsilon = k_B T_1/[(\gamma - 1)m]$. At the centerline, axisymmetric conditions are enforced, *i.e.*, $\partial\Psi/\partial r = 0$, where Ψ is either ρ, u_z or ϵ, and $u_r = 0$. At the outer edges of the computational domain, flow continuation conditions are applied, *i.e.*, $\partial\Psi/\partial z = 0$ for the outer edge in

the z direction, and $\partial\Psi/\partial r = 0$ for the outer edge in the r direction, where Ψ is either ρ, u_r, u_z or ϵ.

Solution Approach

An approximate, quasi-one-dimensional conduction model has been developed to simulate the heat diffusion inside the solid. The development and the numerical solution of this model are described in detail elsewhere[18]. After the temperature field of the solid is found, the conservation equations of mass, momentum and energy of the discontinuity layer can then be solved using simple iterative procedure to provide the boundary conditions for the expansion process.

The governing equation of the expansion process in 2-D axisymmetric coordinates can be written in a generic form given by[19]

$$\frac{\partial U}{\partial t} + \frac{\partial F}{\partial r} + \frac{\partial G}{\partial z} = S, \tag{20}$$

where U is a vector of unknowns, F and G are flux vectors, and S is the source

vector. They are given by

$$U = r\begin{Bmatrix} \rho \\ \rho u_r \\ \rho u_z \\ \rho \epsilon \end{Bmatrix}, F = r\begin{Bmatrix} \rho u_r \\ \rho u_r u_r + P \\ \rho u_r u_z \\ \rho u_r \epsilon + P u_r \end{Bmatrix},$$

and

$$G = r\begin{Bmatrix} \rho u_z \\ \rho u_z u_r \\ \rho u_z u_z + P \\ \rho u_z \epsilon + P u_z \end{Bmatrix}, S = \begin{Bmatrix} 0 \\ P \\ 0 \\ \Lambda + W_l \end{Bmatrix}$$

Because there are sharp gradients in flow fields with shock waves, numerical dissipation is needed to attenuate numerical errors of small wavelengths. The truncation errors, introduced during the discretization of the governing equation, can be interpreted as sources of numerical dissipation and dispersion. A standard upwind scheme should provide strong enough dissipation for most flow problems. However, one must first establish the direction of the characteristic velocity, when the upwind scheme is applied. The flux vector splitting proposed by van Leer [14,15] is a simple way to implement upwind differencing and is briefly described

in the following. The flux vector, $e.g.$, F, is split into forward and backward flux components F^+ and F^- in terms of the local one-dimensional Mach number $M_r = u_r/a$, where a is the local speed of sound. For supersonic flow, $i.e.$, $|M_r| \geq 1$, we have[15]

$$F^+ = F, F^- = 0 \quad \text{for} \quad M_r \geq 1 \tag{21}$$

$$F^+ = 0, F^- = F \quad \text{for} \quad M_r \leq -1. \tag{22}$$

For subsonic flow $|M_r| < 1$,

$$F^{\pm} = r \left\{ \begin{array}{l} f_1^{\pm} \\ f_1^{\pm}[(\gamma-1)u_r \pm 2a]/\gamma \\ f_1^{\pm} u_z \\ f_1^{\pm}\{[(\gamma-1)u_r \pm 2a]^2/[2(\gamma^2-1)] + u_z^2/2\} \end{array} \right\},$$

where

$$f_1^{\pm} = \pm\rho a[(M_r \pm 1)/2]^2. \tag{23}$$

The spatial derivatives of the flux vectors are approximated with backward and

forward differencing using the MUSCL (Monotone Upstream-centered Scheme for Conservation Laws) approach. The approximation of $\partial F/\partial r$ is given by

$$\frac{\partial F}{\partial r} = \frac{1}{\Delta r}[F^+(U^-_{i+1/2}) - F^+(U^-_{i-1/2}) + F^-(U^+_{i+1/2}) - F^-(U^+_{i-1/2})], \quad (24)$$

where the notation $F^\pm(U^\pm)$ denotes $F^\pm$ evaluated at $U^\pm$. $U^\pm$ is given by[20]

$$U^-_{i+1/2} = U_i + \{s/4[(1-\kappa s)\Delta_- + (1+\kappa s)\Delta_+]\}_i, \quad (25)$$

$$U^+_{i+1/2} = U_{i+1} - \{s/4[(1-\kappa s)\Delta_+ + (1+\kappa s)\Delta_-]\}_{i+1}, \quad (26)$$

where

$$\Delta_- = U_{i+1} - U_i, \quad (27)$$

$$\Delta_+ = U_i - U_{i-1}, \quad (28)$$

The spatial differencing is of one-sided second order accuracy when $\kappa = 1$. It is of upwind-biased second order accuracy and third order accuracy when $\kappa = 0$ and $\kappa = 1/3$, respectively. s is the limiter, which governs the accuracy of the approximation. When $s = 0$, the approximation is of first order accuracy. When

$s = 1$, the approximation has the order of accuracy that is determined by κ. The limiter is introduced to locate regions where the solution is discontinuous, such as shock waves, and is required to eliminate oscillations in those regions, and is given by

$$s = \frac{2\Delta_+\Delta_- + \epsilon}{(\Delta_+)^2 + (\Delta_-)^2 + \epsilon}, \tag{29}$$

where ϵ is a small number ($\epsilon = 10^{-9}$) to prevent division by zero in regions of null gradient.

A two-step Runge-Kutta explicit scheme is used to solve the conservation equations, given by

$$U^* = U^n - \frac{1}{2}\Delta t \left(\frac{\partial F}{\partial r} + \frac{\partial G}{\partial z} - S\right)^n, \tag{30}$$

$$U^{n+1} = U^n - \Delta t \left(\frac{\partial F}{\partial r} + \frac{\partial G}{\partial z} - S\right)^*, \tag{31}$$

where the superscripts n and $n+1$ stand for the vectors at time steps n and $n+1$, respectively, and the superscript $*$ implies an intermediate step. The variable vector at the intermediate time step $*$ is first calculated. The flux vectors and source vector are updated to the intermediate time step $*$. Finally, the variable

vector at the new time step $n+1$ is computed.

A test case was calculated to verify the validity of the numerical algorithm, namely, one-dimensional high temperature and high pressure vapor expanding adiabatically into quiescent air. The flow conditions used in the simulation are listed in Table 1. The results of the numerical simulation at 200 ns are shown in Figure 2. A shock wave can be clearly seen in the figure, which propagates at supersonic speed into the quiescent air (section 1) and sets up the gas behind it in motion in the direction of the shock wave. In the meantime, a rarefaction wave generated from the quiescent air propagates in the opposite direction into high pressure vapor (section 4). The shock wave and the rarefaction wave interact in such a manner as to establish a common pressure and velocity for the gas downstream of these waves (section 2 and 3). While flow across the rarefaction wave is isentropic, flow across the shock wave is highly irreversible and follows the Rankine-Hugoniot relation. Theoretical results for this type of problems can be found in any standard compressible fluid mechanics textbook, $e.g.$,[21]. Comparisons were made with theoretical results. The numerical results agree well with theoretical results in the rarefaction wave region. While the theoretical shock wave front shows very steep change in pressure, density, speed and temperature, the shock wave is smeared in the numerical simulation. This is due to the numer-

ical dissipation inherent in the flux vector splitting scheme.

Results and Discussion

Simulations were performed for graphite subject to the heating of a KrF excimer laser with a wavelength of 248 nm. The graphite sample is irradiated by a laser pulse of 10 ns duration, 0.1J per pulse and laser radius w_g of 1000 μm, $i.e.$, parameters typically found during pulsed laser deposition of diamond-like-carbon thin films[22]. The ambient air has a temperature of 300 K and density of $1.16\times10^{-}2$ kg/m^3, which correpond to a vaccum of base pressure of 1 kPa. The material properties of graphite listed in Table 2 were used for this simulation. Additionally, the ratio of specific heats γ is taken as 1.67, and the ionization energy χ_Z of graphite is taken as 1.804×10^{-18} J[23].

Figure 3 to 5 shows the contour plots of the density ρ, pressure P, temperature T, and two velocity components u_r and u_z at three instants of laser operation. The contour plots show clear structures of a shock wave. After the evaporation starts, a series of compression waves rapidly coalesce into a shock wave. The shock wave front, pushed by the high temperature and high pressure vapor resulting from the laser heating of the solid, expands at supersonic speed. An expansion wave originating from the quiescent ambient air moves toward the bottom surface and center simultaneously. This results in a flow field that has a smooth gradient

at the center and the bottom part and a sharp gradient at the top and outer edges. The contour plots have disk-like shapes at 2 ns. As the expansion of the vapor progresses, the contours take dome-like shapes at 5 ns and 10 ns. These contour plots show that the shock wave expansion is predominantly one-dimensional and is dominated by the expansion in the z-direction. At any instant, the density and the pressure of the vapor is the highest at the solid-vapor interface. They decrease monotonously as the vapor moves downstream. The temperature of the vapor decreases at first as the vapor expands and starts to increase as the vapor moves closer to the edge of the shock wave. The temperature reaches its peak at slightly under the shock wave front. The sharp rise of the temperature under the shock wave front is due to both shock wave heating and the absorption of the laser light. At the onset of the expansion process, a small fraction of the high temperature core has a temperature exceeding 240,000 K. As the vapor expands, the temperature decreases substantially. The local velocity in the r-direction u_r increases as the vapor expands laterally from the center and reaches its peak at the outer edge of the shock wave. It then sharply decreases to 0 beyond the shock wave front. At 2 ns u_r is below 400 m/s everywhere. It increases rapidly and exceeds 800 m/s at the outer edge of the shock wave at 5 ns. The local velocity u_r then increases further and reaches a peak value of 1000 m/s at 10 ns. It can be seen that there

is a core region near the centerline, where u_r increases from roughyly 300 m/s at 2 ns to 700 m/s at 10 ns. It should be noted that this core region is spurious numerical results due to the sharp gradient of the shock wave. The local velocity in the z-direction u_z behaves similarly. It increases as the vapor expands upward and reaches its peak under the top edge of the shock wave. The local velocity u_z is the highest within a core region that is slightly under the shock wave front. The peak velocity in the z-direction decreases slightly as the expansion progresses.

The temperature and pressure profiles of the vapor at the centerline are shown in Figure 6. The figures show clearly that the expanding vapor at first experiences an isentropic rarefaction wave, where both the temperature and pressure decrease as the vapor moves forward. The vapor then encounters a highly irreversible shock wave, where the pressure decreases sharply and the temperature rises due to shock wave heating. The structures of the temperature and pressure profiles are similar to those of a 1-D flow shown in Figure 2. The similarity confirms the earlier statement that the shock wave expansion is predominantly one-dimensional.

The locations of the wave front at different instants indicate that the high temperature and high pressure vapor expands upward at a very high speed at the onset of the evaporation. As the expansion goes on, the speed of the shock wave decreases slightly. An average upward velocity of approximately 23000 m/s is

recorded at 10 ns. The reason for such hyper speed is that the vapor expansion is powered not only by high pressure and high temperature vapor coming from the receding solid surface, but also by absorption of laser light by plasma which provides additional energy, and fuels further expansion of the vapor. Experimental investigation indicates that the shock wave front moves at a speed between 2000 m/s to 8000 m/s during laser heating of solid at atmospheric pressure[24]. Since the current numerical simulations were run with a fairly low background pressure which is known to facilitate the expansion speed of the shock wave[21], and the physical properties of the vapor/plasma were assumed to be independent of temperature, the numerical results agree qualitatively with experimental results.

An investigation of effects of laser power on the evaporation process was carried out as well. The contour plots of laser induced vapor at two different laser power levers are presented in Figure 7 and Figure 8. A graphite target is irradiated by a KrF laser pulse of 10 ns duration, and laser radius w_g of 1000 μm. However, the laser energy per pulse are 0.05 J and 0.02 J, respectively. Figure 7 and Figure 8 show the the contour plots of the density ρ, pressure P, temperature T, and two velocity components u_r and u_z after 10 ns of laser operation. The contour plots show very similar shock wave structure to the previous case. While it can be seen that the shock waves propagates at a relatively low speed compared with

higher laser power, the average upward speeds of 19000 m/s and 15000 m/s agree qualitatively with speeds measured in experiments[24]. The density, pressure, temperature and local velocity of the laser induced plasma are all lower than those of previous numerical results.

The number density and the local absorption coefficients at 10 ns are shown in Figure 9. The degree of ionization is estimated using Saha's equation, which indicates that the electron density depends on both vapor density and electron temperature. When the electron temperature reaches the order of χ_Z/k_B, the electron density is a very strong function of electron temperature. It can be seen from Figure 5 that the vapor density is low under the shock wave front, where the electron temperature reaches its peak. By virtue of this high electron temperature, and despite the relatively low vapor density, the electron density approaches its peak value at the shock wave front. The absorption coefficient of the plasma cloud is modeled using inverse Bremsstrahlung absorption. Because the absorption coefficient depends strongly on the electron density, it is the largest at the shock wave front, where the electron density approaches its peak value. The numerical values in Figure 9 also indicate that the laser induced plasma has fairly small absorption coefficients, which is partly due to the short wavelength of KrF excimer laser. The small absorption coefficients of the laser induced plasma indicate that the absorp-

tion of laser light by the plasma is not siginificant.

Conclusions

The laser material interaction of nanosecond duration has been investigated by numerical simulation. A quasi-one-dimensional model is used to simulate heat conduction inside the solid. A discontinuity layer is attached to the receding solid surface. Mass, momentum and energy are conserved across the discontinuity layer. The algebraic equations of mass, momentum and energy conservation are solved simultaneously to provide boundary conditions for the expansion process of high temperature and high pressure vapor. Euler equations are developed to model the expansion and ionization of the vapor phase. The Euler equations are integrated numerically using a Runge-Kutta scheme combined with flux vector splitting. The degree of ionization is computed using Saha's equation. The strong absorption of laser light is modeled using inverse bremsstrahlung absorption. Numerical simulations of laser heating processes are conducted for graphite substrates subject to KrF laser irradiation.

The simulation results indicate: i) The contour plots of plasma density, pressure temperature and speed all show distinctive shock wave structure. ii) The expansion of laser induced plasma is predominantly one-dimensional. iii) The high temperature and high pressure plasma expands with an average speed of

15000-23000 m/s, which agree qualitatively with experimental results. iv) Substantial ionization occurs in the laser induced vapor during typical pulsed laser deposition. v) The laser induced plasma has a small absorption coefficient. The shielding of laser light from the laser target is not significant for short wavelength laser.

References

[1]Baller, T. S., van Veen, G. N. A., and van Hal, H., *Applied Physics A*, Vol. 46, 1988, p. 215.

[2]Sankur, H. and Cheung, J., *Applied Physics A*, Vol. 47, 1988, p. 271.

[3]Koivusaari, K. J., Levoska, J., and Lepavuori, S., *Journal of Applied Physics*, Vol. 85, 1999, pp. 2915–2920.

[4]Ready, J. F., *Effects of High-Power Laser Radiation*, Academic Press, 1971.

[5]Bloembergen, N., In *Material Research Society Symposium Proceeding*, Vol. 51, 1985, pp. 3–13.

[6]Anisimov, S., *Soviet Physics JEPT*, Vol. 27, 1968, pp. 182–183.

[7]Knight, C. J., *AIAA Journal*, Vol. 17, 1979, pp. 519–523.

[8]Krokhin, N., In Caldirola, P. and Knoepfel, H., eds., *Physics of High Energy Density*, Academic Press, 1971, pp. 278–305.

[9]*Material Research Society Symposium Proceedings*, Material Research Society.

[10]Hora, H., ed., *Workshop on Laser Interaction and Related Plasma Phenomena*, Plenum.

[11]Ho, J. R., Grigoropoulos, C. P., and Humphrey, J. A. C., *Journal of Applied Physics*, Vol. 78, 1995, pp. 4696–4709.

[12]Ho, J. R., Grigoropoulos, C. P., and Humphrey, J. A. C., *Journal of Applied Physics*, Vol. 79, 1996, pp. 7205–7215.

[13]Tokarev, V. N., Lunney, J. G., Marine, W., and Sentis, M., *Journal of Applied Physics*, Vol. 78, 1995, pp. 1241–1246.

[14]van Leer, B., In *Lecture Notes in Physice*, Springer, Vol. 170, 1982, pp. 507–512.

[15]Anderson, W. K., Thomas, J. L., and van Leer, B., *AIAA Journal*, Vol. 24, 1986, pp. 1453–1460.

[16]Hughes, T. P., *Plasmas and Laser Light*, John Wiley & sons, 1975.

[17]Shearer, J. W. and Barnes, W. S., In Hora, H., ed., *Laser Interaction and Related Plasma Phenomena*, Vol. 1, Plenum, 1971, pp. 307–338.

[18]Zhang, Z., "Numerical Simulation of Short-Pulsed Laser Processing of Materials", *Numerical Heat Transfer A*., (in press).

[19]Holst, T. L., "Numerical Solution of Axisymmetric Boattail Fields with Plume Simulators", AIAA paper 77-224, 1977.

[20]Mulder, W. A. and Van Leer, B., "Implicit Upwind Methods for the Euler Equations", AIAA paper 83-1930, 1983.

[21]Anderson, J. D., *Modern Compressible Flow with Historical Perspective*, McGraw-Hill, 1982.

[22]Tabbal, M., Merel, P., Chaker, M., El Khakani, M. A., Herbert, E. G., Lucas, B. N., and O'Hern, M. E., *Journal of Applied Physics*, Vol. 85, 1999, pp. 3860–3865.

[23]Radzig, A. A. and Shustryakov, V. M., In Grigoriev, I. S. and Meilikhov, E. Z., eds., *Handbook of Physical Quantities*, CRC Press, 1997, pp. 515–522.

[24]Song, K. H. and Xu, X., *Applied Surface Science*, Vol. 127-129, 1998, pp.

111–116.

List of Table Captions

Table 1: Flow conditions of the 1-D test problem

	T(K)	P(MPa)	ρ(kg/m^3)	v(m/s)
Inlet	7651	148.7	93.9	1623
Background	600	1.24	10	0

Table 2: Material properties of graphite

T_b(K)	α_s(m^2/s)	ρ_o(kg/m^3)	L(J/kg)	c_p(J/kgK)	l(μm)
4000	5×10^{-6}	1.73×10^3	34.5×10^6	2090	0.1

List of Figure Captions

Figure 1: Schematic and coordinate system of laser machining process

Figure 2: Comparisons between theoretical and numerical predictions of pressure, density, speed and temperature profile of an adiabatic one-dimensional gas expansion process

Figure 3: Numerical predictions of density, pressure, temperature and velocity field of a laser induced plasma after 2 ns of laser operation with 0.1J of energy per pulse

Figure 4: Numerical predictions of density, pressure, temperature and velocity field of a laser induced plasma after 5 ns of laser operation with 0.1J of energy per pulse

Figure 5: Numerical predictions of density, pressure, temperature and velocity field of a laser induced plasma after 10 ns of laser operation with 0.1J of energy per pulse

Figure 6: Temperature and pressure profiles at the centerline at several instants

Figure 7: Numerical predictions of density, pressure, temperature and velocity

field of a laser induced plasma after 10 ns of laser operation with 0.05J of energy per pulse

Figure 8: Numerical predictions of density, pressure, temperature and velocity field of a laser induced plasma after 10 ns of laser operation with 0.02J of energy per pulse

Figure 9: Numerical predictions of electron density and absorption coefficient of a laser induced plasma at 10 ns

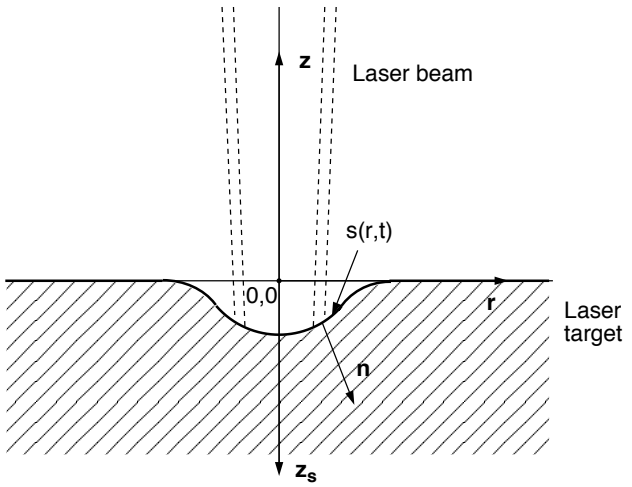

Figure 1: Schematic and coordinate system of laser machining process

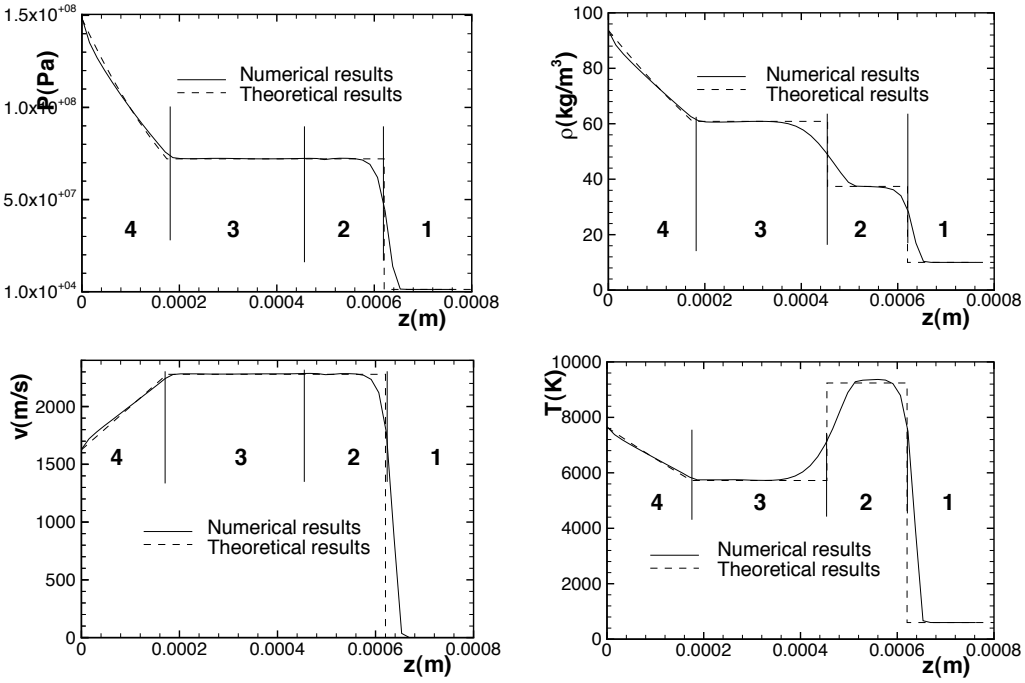

Figure 2: Comparisons between theoretical and numerical predictions of pressure, density, speed and temperature profile of an adiabatic one-dimensional gas expansion process

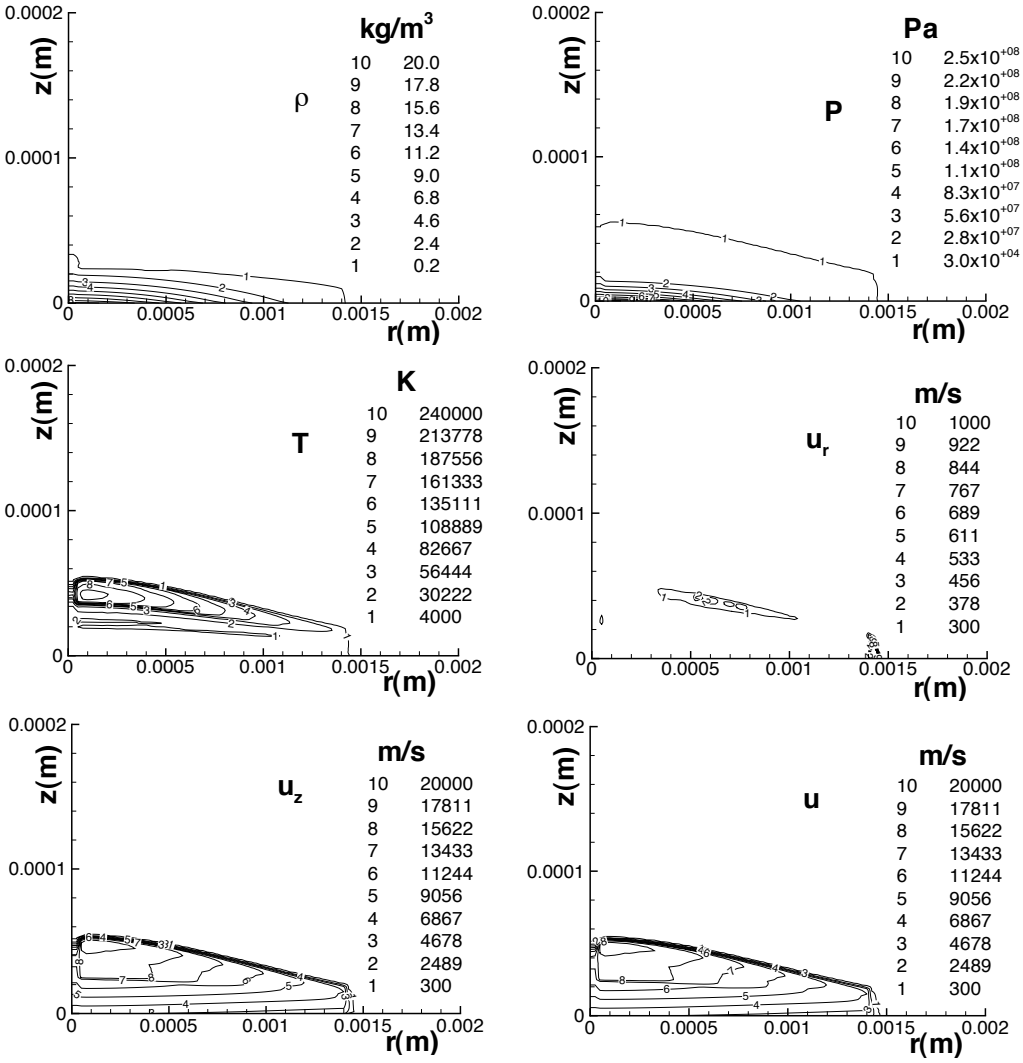

Figure 3: Numerical predictions of density, pressure, temperature and velocity field of a laser induced plasma after 2 ns of laser operation with 0.1J of energy per pulse

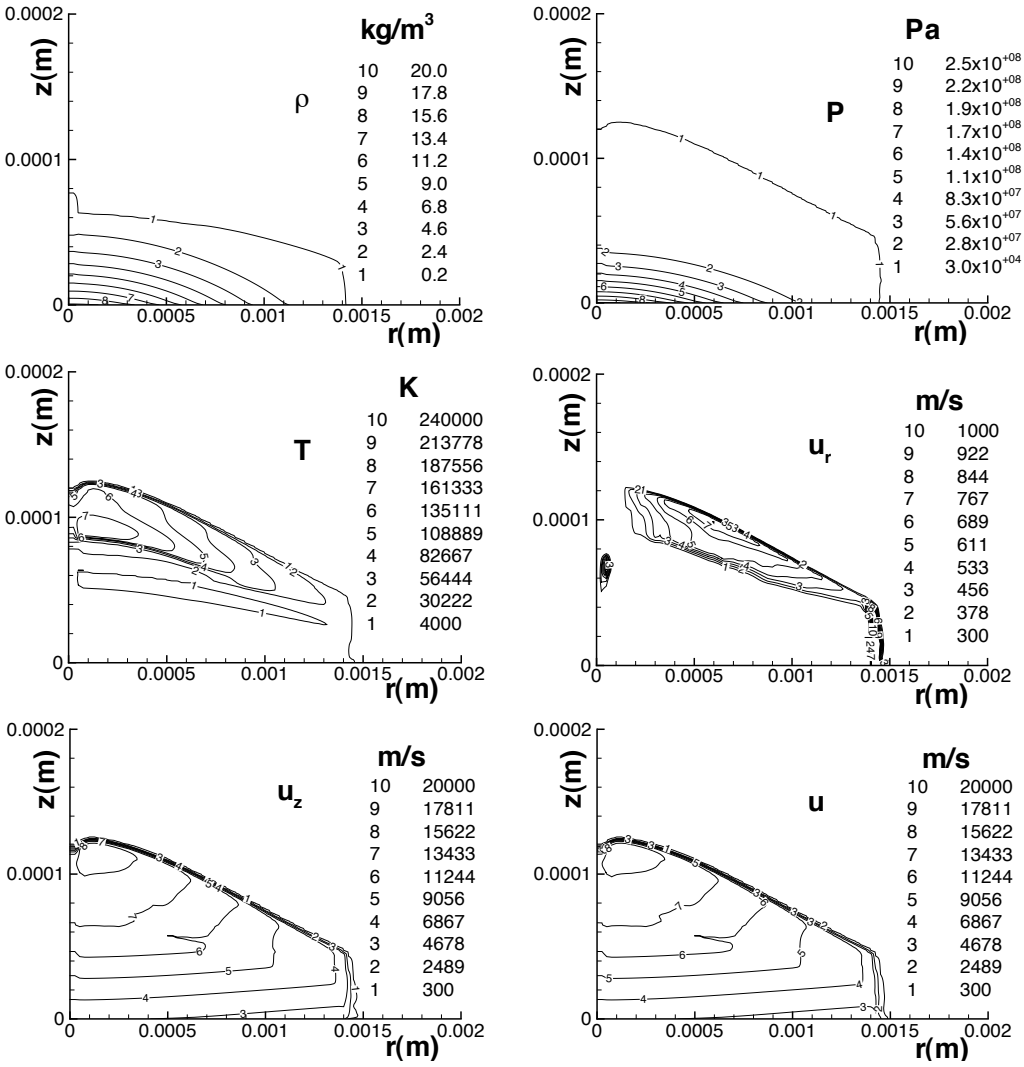

Figure 4: Numerical predictions of density, pressure, temperature and velocity field of a laser induced plasma after 5 ns of laser operation with 0.1J of energy per pulse

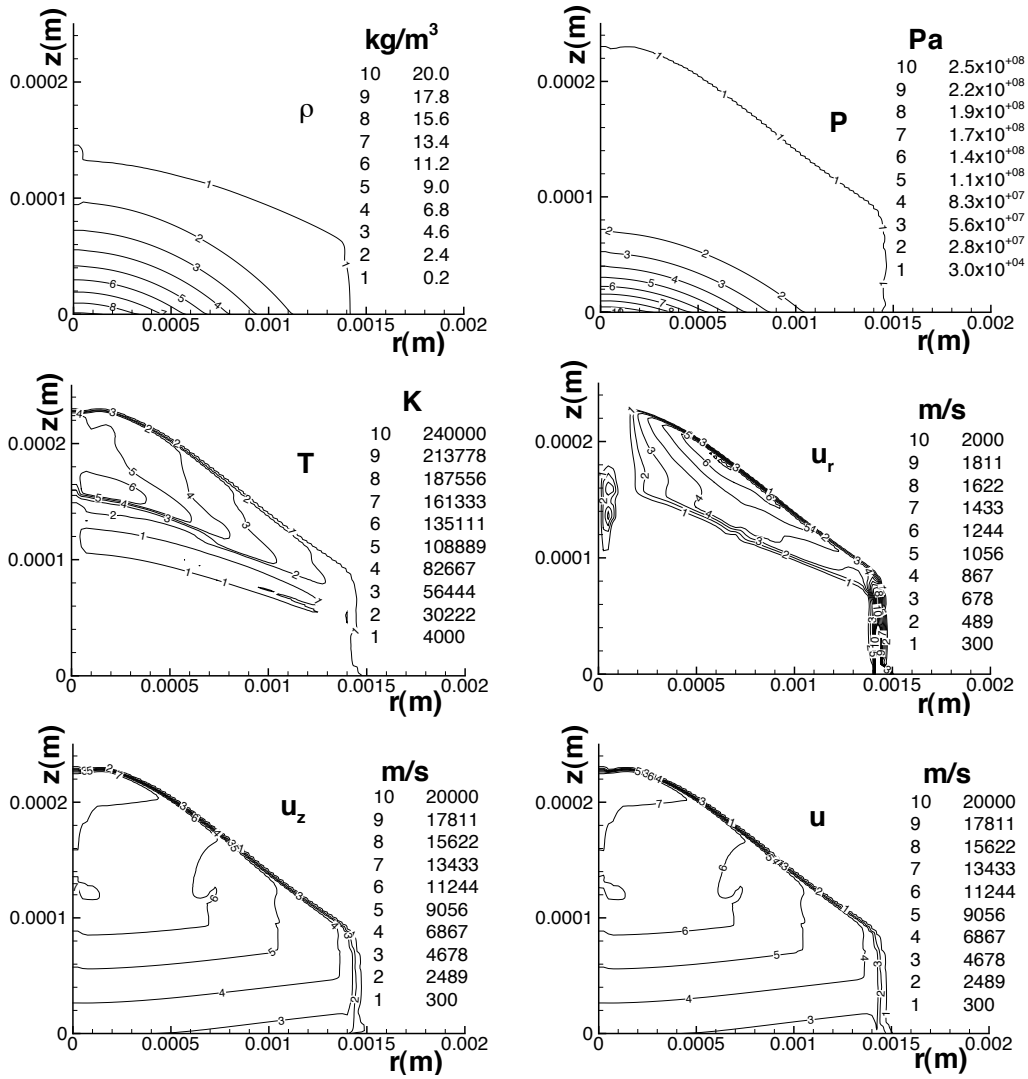

Figure 5: Numerical predictions of density, pressure, temperature and velocity field of a laser induced plasma after 10 ns of laser operation with 0.1J of energy per pulse

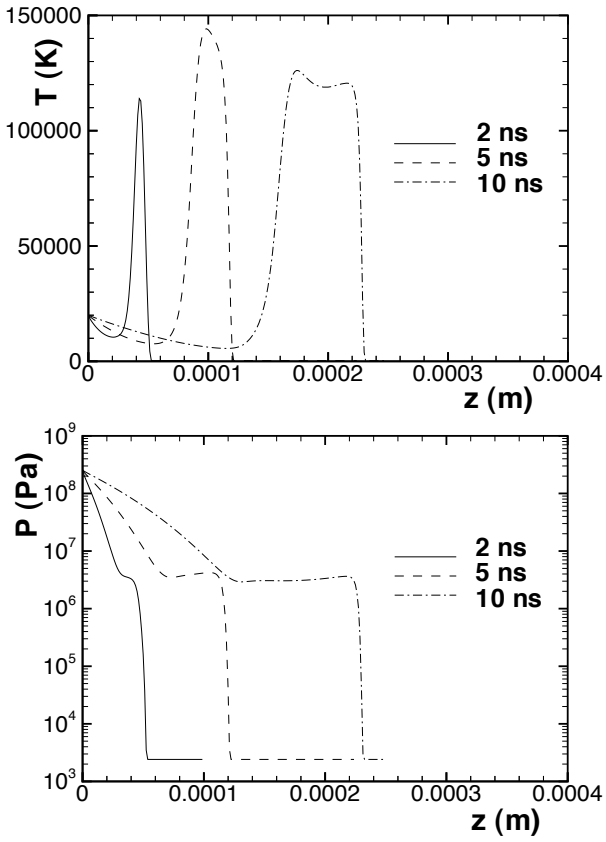

Figure 6: Temperature and pressure profiles at the centerline at several instants

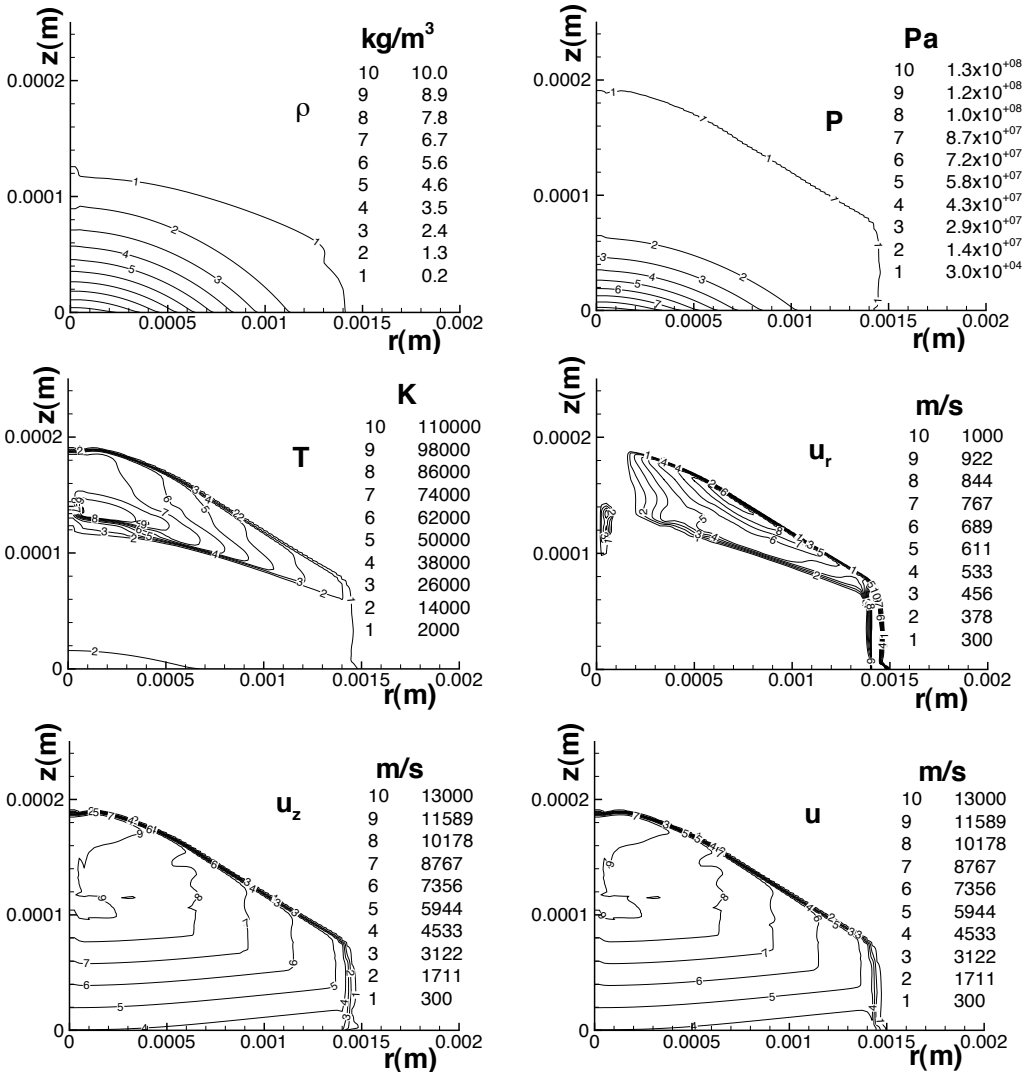

Figure 7: Numerical predictions of density, pressure, temperature and velocity field of a laser induced plasma after 10 ns of laser operation with 0.05J of energy per pulse

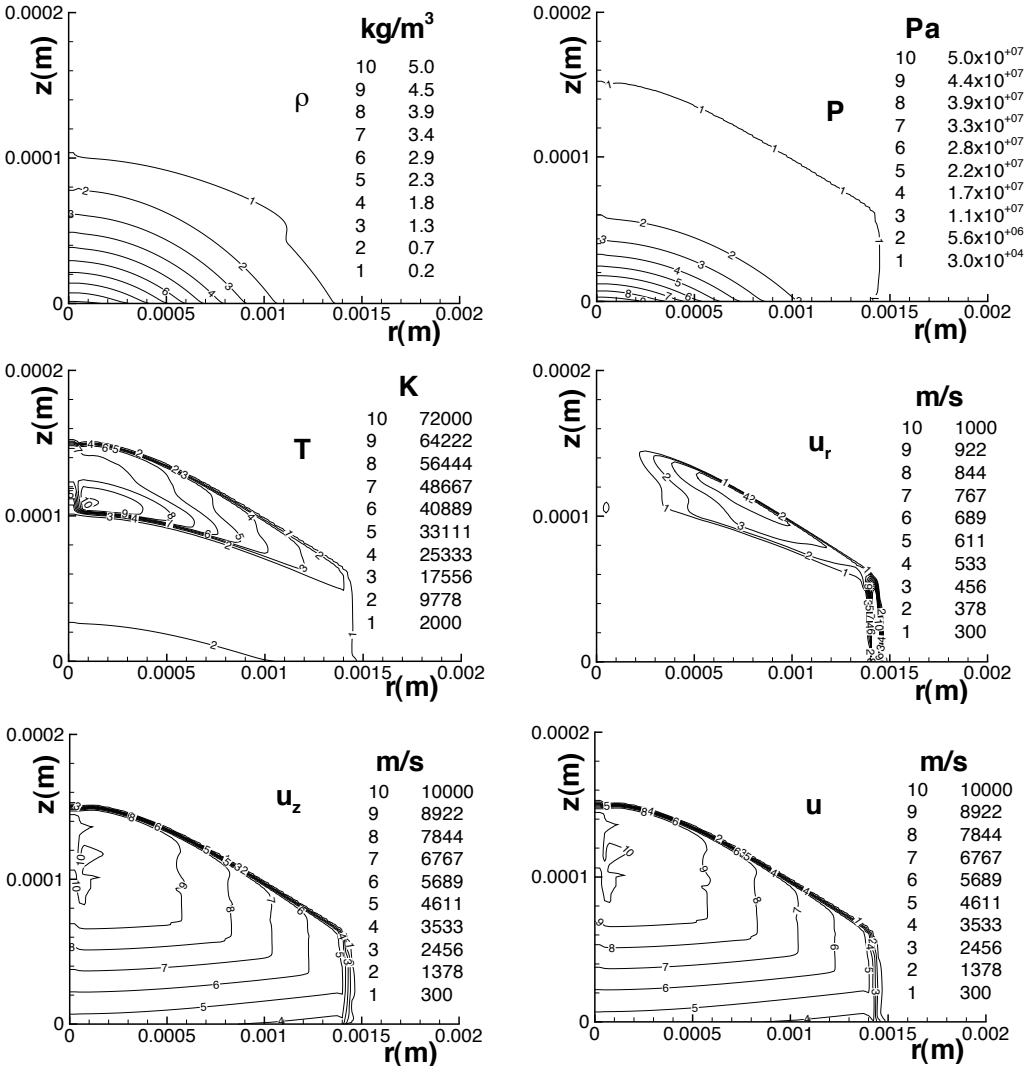

Figure 8: Numerical predictions of density, pressure, temperature and velocity field of a laser induced plasma after 10 ns of laser operation with 0.02J of energy per pulse

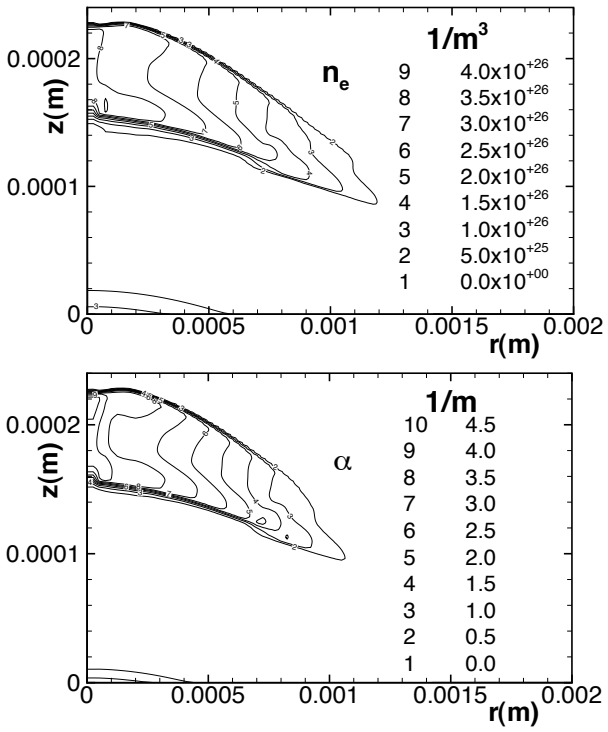

Figure 9: Numerical predictions of electron density and absorption coefficient of a laser induced plasma at 10 ns